Contents lists available at ScienceDirect

Applied Catalysis B: Environmental

Electrochemical simultaneous treatment approach: Electro-reduction of CO_2 at Pt/PANI@ZnO paired with wastewater electro-oxidation over PbO_2

Sina Khalili, Abbas Afkhami [*], Tayyebeh Madrakian

Faculty of Chemistry, Bu-Ali Sina University, Hamedan 6517838695, Iran

ARTICLE INFO	ABSTRACT
	The electro-reduction of CO_2 paired with wastewater electro-oxidation processes is a promising method for producing value-added products and decreasing energy consumption. In an H-type cell, the electrocatalytic mineralization of AMD 10B in an aqueous medium over novel β-PbO_2 anode paired with the CO_2 electrocatalytic reduction converts to methanol and formic acid at Pt/PANI@ZnO cathode. The proposed anode electrode showed a very high surface-to-volume ratio, high-performance electrocatalytic degradation, and a long service lifetime. Experimental results indicate in the anode compartment, a good COD removal efficiency (93%) and the lowest specific energy consumption, 4.6 kWh m^{-3} were obtained. Simultaneously, results obtained from the catholyte analysis showed Faradaic efficiency of 57% and 41% with a total cathodic energy efficiency of 34% at 15 mA cm^{-2} for methanol and formic acid, respectively. The lowest cell voltage was obtained (3.92 V) by using NaCl in the anolyte.

1. Introduction

The continuous growth of human industrial activities has resulted in a huge spike of carbon dioxide (CO_2) emissions, an annual average rise of 1.9 parts per million (ppm), into the atmosphere. The global warming phenomenon is the immediate consequence of CO_2 emissions [1]. The development of cost-effective methods that reduce or convert atmospheric CO_2 into high-value chemical materials is of vital importance for humanity's survival. Conversion of the captured CO_2 into valuable materials such as formic acid, methanol, methane, and so forth, has been the main scientific challenge [2–4].

The CO_2 electro-reduction methods can be divided into two categories. First, the direct CO_2 reduction to the CO° intermediate, which, depending on the reaction medium, can be followed by further electron transfer (2–6 electrons). The second category is electro-carboxylation reactions [5,6]. However, CO_2 electro-reduction still has many limitations and challenges that limit industrial application. One of the significant limitations of CO_2 electro-reduction is the high thermodynamic and kinetic stability of CO_2 molecules. To overcome this limitation, high cathodic overvoltage is required to run the reduction process [7,8]. To date, many reports are available in the literature for decreasing the cathodic overvoltage via the aqueous and non-aqueous media, the type of electrolyte, the effect of the pH, cell design, and the effect of the

electrocatalyst size and structure [9–17]. Despite much progress, CO_2 electro-reduction in an aqueous media is generally paired with oxygen evolution reaction (OER) in an anodic process and produces low-value O_2 gas on a large industrial scale. Assessing the balance between energy consumption and production yield is significant for CO_2 conversion. The CO_2 electrochemical reduction paired with a helpful oxidation process could enable the removal of this imbalance. Electrochemical oxidation processes have been used for years as promising candidates for balancing energy combustion because of their high-cost effectiveness, high energy efficiency, and versatility [18,19].

These techniques appealing ecological and economic opportunities. However, the appropriate choice of the anodic reaction owing to the production of high-value chemical materials in anolyte has recently received considerable attention. Recent research is being focused on the synergetic optimization of the overall cell reaction. [19–21]. The CO_2 electrochemical reduction has been paired with several reactions with lower overvoltage requirements; among these reactions, the water pollution degradation by the electro-oxidation process is the high-potential candidate for replacing the anodic reaction [22]. A new trend in the paired CO_2 conversion process is the water pollution electro-oxidation at the anodic cell and the CO_2 reduction in the cathodic cell by using a divided cell. [23].

The fabricated organic N-containing polymer layers on the electrode

---

surface such as polyaniline (PANI) and polypyridine (PPY) show an improvement in the product selectivity and decreased cathodic overvoltage in CO_2 reduction. N-containing polymers can trap $CO^{\cdot}$ intermediate molecules with a strong Lewis acid-base interaction at the electrode surface [24,25]. The synthesis of hybrid materials based on N-containing polymers with doping of different nanoparticles such as Pd, Cu, ZnO, and titanium dioxide (TiO_2) has received special attention due to their catalytic properties [26–28]. ZnO is an amphoteric oxide that can interact with $CO^{\cdot}$ intermediate and keep it on the surface to cause the continuity of more electron transfer. The conductive organic composite PANI@ZnO (with different percentages of ZnO) represents a decrease in the overpotential and enhances the catalytic activity of the cathodic process for CO_2 electro-reduction.

The azo dye amido black 10B (AMD 10B) is chosen as a water pollutant because of its structure (aromatic derivative parts), and for the first time, an electrochemical mechanism model is proposed to better understand the electrochemical performance. The PbO_2 electrode can degrade recalcitrant organic pollution by in-situ production of strong oxidants OH radical during water electrolysis. A novel β-PbO_2 electrode was fabricated for the AMD10 oxidation process in an aqueous solution. Several additives were introduced into the β-PbO_2 electrolyte for highly stable deposition and enhancement of electrode oxidation performance [29–32]. A recent study reported, the effect of copper (Cu) ion additives on the β-PbO_2 electrolytes, which avoid nitrate reduction and Pb deposition on the cathode electrode [33].

Herein, for the first time, the fine copper powder was used as a source of Cu ions that can release Cu^{2+} slowly in an oxidation process at the anode surface or acidic electrolyte medium during the reaction. It also demonstrated that the novel PbO_2 electrode has a highly dense surface area and high electrocatalytic activity. In addition, we proved that replacing OER with dye degeneration in the anodic compartment results in decreased energy consumption during simultaneous production at the cathode and anode. This study also demonstrated the performance of cathodic and anodic electrodes for paired electrolysis.

2. Experimental section

2.1. Chemicals

All chemical compounds were purchased from Merck Chemical Company (Darmstadt, Germany) and used without further purification. Aniline monomer (Sigma–Aldrich Company) was distilled and stored in the dark at 4 °C before use in the electrochemical process. Zinc oxide (ZnO) nanoparticles with 10–20 nm particles size were purchased from US Nano Company (US NANO, USA). The Nafion-117 membrane was purchased from DuPont Company (USA). To adjust the desired pH, a phosphate buffer solution was made from phosphoric acid (0.2 M) with a suitable amount of NaOH. To prepare working solutions, deionized water was used throughout the experiments.

2.2. Apparatus

Cyclic voltammetry (CV) and linear sweep voltammetry (LSV) were performed using an Autolab PGSTAT 302 N model potentiostat/galvanostat (Eco-Chemie, Netherland) that was controlled by NOVA 1.11 software. For paired reactions, an H-Type cell was used. A two-compartment gas-tight electrochemical cell with a piece of Nafion-117 membrane was applied for all electrochemistry paired systems as a separator. The graphite plate (GP) and stainless-steel plate (SSP) with a thickness of 1 mm × 20 mm × 30 mm, with an effective surface area of about 13 cm^2 were used as the anode and cathode electrodes, respectively. Each cell compartment contained 50 mL of an aqueous solution of 0.5 M $KHCO_3$ (pH=5.0) as catholyte and 0.5 M NaCl as anolyte (pH=5.0). In the cathodic compartment, a leak-free Ag/AgCl electrode was used as the reference electrode (3.0 M KCl). To investigate the electrochemical behavior of AMD 10B, a bare glassy carbon electrode

(Azar electrode Co., Iran, d = 2.0 mm) was employed as the working electrode. A platinum rod and a commercial Ag/AgCl were used as the auxiliary and reference electrodes, respectively. A Metrohm 713 pH meter was used to adjust the pH of the phosphate buffer solutions. The surface morphologies were observed using field emission scanning electron microscopy (FESEM; TESCAN MIRA3 LMU, Czech Republic). X-ray diffraction (XRD) patterns were recorded using a GNR, APD 2000 PRO diffractometer (Italy) under a Cu K_α radiation wavelength of 1.541874 Å to study the crystal phase. Furthermore, the absorption spectra were investigated using an Agilent diode array UV–vis spectrophotometer (Agilent, USA). The gas chromatography (GC) system controlled by the Chemstation software equipped with a 7653B automatic injector consisted of an Agilent 7890 A gas chromatograph (Agilent Technologies, Waldbronn, Germany) coupled to a flame ionization detector (FID). The surface compositions and oxidation states of the as-fabricated electrodes were conducted via X-ray photoelectron spectroscopy (XPS, ESCALAB 250Xi, Thermo Fisher, United States). Inductively coupled plasma optical emission spectrometry (ICP-OES, Spectro Arcos, Germany) was used for the determination of Cu in the PbO_2 matrix.

2.3. Fabrication of electrodes

2.3.1. Cathode electrode

The GP as a cathode electrode was mechanically polished with 600, 800, and 1200-grit sandpapers and washed thoroughly with deionized water. Then GP was electropolished before each experiment by CV (15 cycles) between − 1.5 V and + 1.5 V vs. Ag/AgCl in a 0.1 M H_2SO_4 solution. Afterward, the PANI layer was grown on the GP surface by scanning the electrode potential from − 0.2 V to + 0.8 V vs. Ag/AgCl in a solution containing 0.1 M aniline + 0.5 M H_2SO_4 and 0.01 M $LiClO_4$ at a scan rate of 100 mV s^{-1} for 20 cycles under the nitrogen purging. To prepare the PANI@ZnO composite on the GP surface, the PANI@ZnO layer was synthesized in a solution containing 0.1 M aniline, 0.5 M H_2SO_4, 0.01 M $LiClO_4$ and different concentrations of ZnO nanoparticles powder (20, 40, and 60 mg L^{-1}) by CV method in the potential range between − 0.2 to + 0.8 V vs. Ag/AgCl at a scan rate of 100 mV s^{-1} for 25 cycles under the nitrogen purging. The electro-deposition of platinum nanoparticles on the PANI and PANI@ZnO surfaces (denoted as Pt/PANI/GP and Pt/PANI@ZnO, respectively) was performed through the application of constant potential (−0.20 V vs. Ag/AgCl) for 15 min in an aqueous solution containing 150 μM $PtCl_2$ and 0.1 M phosphate buffer (pH = 7.0) under nitrogen purging. Afterward, the electrode was rinsed with deionized water and placed in the electrochemical cell.

2.3.2. Anode electrode

The SSP as the anode electrode was mechanically polished (800 and 1200-grit sandpapers) and electropolished (CV between −2 and +2 V in 0.5 M H_2SO_4 solution). The pretreatment of the electrode substrates was preceded by ultrasonic cleaning in the 1 M NaOH solution for 15 min to remove organic impurities from the plate. Then the SSP was rinsed with deionized water. Afterward, the electrodes were withdrawn from the deionized water solutions and etched in nitric acid 45% for 5 min to activate the surface of the SSP. The critical parameters for the deposition of the β-PbO_2 layer, including temperature, acid concentration, amount of Cu powder, type of surfactant, and current density, were controlled to obtain desired electrocatalytic performance and high stability. The β-PbO_2 layer on the SSP was prepared using the electrochemical deposition process in a solution composed of 0.5 M HNO_3 + 0.01 M SDS + 0.005 M NaF + 0.5 M $PbNO_3$, and 300 mg L^{-1} Cu fine powder. For the preparation of the best electrodes, PbO_2 was deposited at the optimum conditions, i.e. at a temperature of 80 °C and a current density of 12 mA cm^{-2} for 90 min with continuous stirring. The β-PbO_2 electrodes in Cu^{2+} free solution and solution containing Cu^{2+} ion were synthesized according to the previously reported method in order to investigate the performance of Cu-powder and the morphology of β-PbO_2 [33] (Scheme
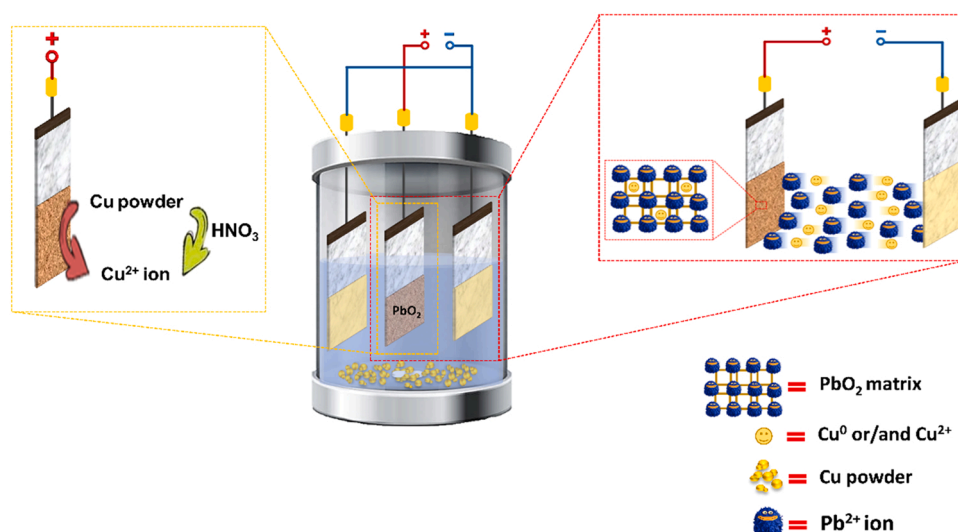
Scheme 1. A scheme of the PbO₂ electrodeposition process.

1).

3. Results and discussion

3.1. Characterizations of the anodic electrodes

FESEM, XRD, and LSV were used to identify the surface morphology, crystal structure, and electrochemical activity of the different anode electrodes. The influence of the different electrodeposition solutions on the surface morphology of the PbO₂ layer was studied by FESEM. As shown in Fig. 1 (I, II, and III), FESEM images illustrate the surface morphology of the PbO₂ layer in the different electrodeposition solutions including Cu^{2+}-free solution, a solution containing Cu^{2+} ions, and Cu-powder. The effect of the source of Cu ions on the structure and shape of PbO₂ layers can be perceived from the FESEM images. FESEM images in Fig. 1 (I-III) were compared, and a noticeable decrease in crystal sizes and an increase in density was observed. Therefore, the presence of a Cu source can lead to a slow nucleation process near the surface of the electrode. As shown in Fig. 1 (III), the presence of Cu-powder as a Cu source in the electrodeposition solution resulted in a good distribution structure with hexagonal pyramidal morphology having very sharp corners and transparent edges as well as more compact structures as compared to the reported ones [33,34]. The Cu electro-oxidation at the anode surface controls the nucleation growth and orientates the PbO₂ grain structure. The electro-oxidation of Cu-powder passivates the nucleation process. The Cu-powder inhibits the grains from growth and maintains the grain's small size. On the other hand, Cu-powder may cause the pyramid shape of PbO₂ by passive pits or depressions on the anode surface, which has a low potential. Therefore, PbO₂ forces electrodeposition at higher potential surfaces. The nucleation process is stopped by increasing the amount of Cu-powder because most of the energy is used for the oxidation of the Cu-powder. This effect makes the PbO₂ unable to acceptably deposit on the surface, leading to the PbO₂ being brittle. It is well-known that dense and compact structures are favorable for realizing high-performance electrochemical activities, leading to more active sites.

Fig. 1 (IV) shows the XRD patterns of PbO₂ electrodes in different electrodeposition solutions. XRD pattern (a) indicates the crystal structure of the PbO₂ electrode in the Cu-free solution electrolyte. The XRD pattern of PbO₂ shows the main diffraction peaks at $2\Theta = 25.3°$, $31.8°$, $36.1°$, and $48.8°$, corresponding to (110), (101), (200), and (211) planes of β-PbO₂. An interpretation is fully consistent with the standard diffraction peaks (JCPDS 76–0564) [33,34]. Both PbO₂ electrodes synthesized in the electrolyte solutions containing Cu^{2+} ions and Cu-powder appeared in the crystal structures of β-PbO₂, although, the nucleation rates of both PbO₂ electrodes are slightly different. The intensity of the diffraction peak at 25.3° in the XRD pattern of PbO₂ synthesized in the electrolyte solution containing Cu-powder, which is assigned to the (110) plane of β-PbO₂, is larger compared to the intensity of the diffraction peak of PbO₂ synthesized in the electrolyte solution containing Cu^{2+} ion. This result indicates an increase in the crystallinity of the PbO₂ synthesized in the electrolyte solution containing Cu powder. This observation indicates that the nucleation rate of PbO₂ is slow in an electrolyte solution containing Cu powder. This can be described by copper preventing the PbO₂ structure from growing more quickly. As evident, the effect of the controlled release of Cu ions originating from Cu powder within a specific flux in the anode surface can be discerned. This observation was consistent with the FESEM morphology.

The performance of the different PbO₂ substrates in the OER was estimated by the LSV technique. These results show that the overpotential for OER on the PbO₂ electrode synthesized in an electrolyte solution containing Cu-powder is higher than that of the other electrodes, shown in Fig. 1 (V). It is worth noting that the OER occurs extremely at a more positive potential compared to the other electrode. The PbO₂ electrode synthesized in an electrolyte solution containing Cu powder has overvoltage for OER that is suitable for the electro-oxidation treatment of wastewater owing to the generation of reactive oxygen species, including O₃ and H₂O₂.

Additionally, to get data on the stability of the PbO₂ electrode, accelerated lifetime tests were accomplished in strongly acidic electrolyte 3.0 M H₂SO₄ at 500 mA cm^{-2} at room temperature. The working electrode potential during the stability test was monitored periodically. When the measured working potential reached 10 V, the anode was deactivated. Fig. 1 (VI) shows an accelerated lifetime of PbO₂ electrodes synthesized in the electrolyte solution containing Cu^{2+} ion and Cu-powder. From these figures, introducing Cu-powder to the electrolyte can expand the lifetime window of PbO₂ electrodes activated by more than 56 h. As illustrated in Fig. 1 (II, and III), the PbO₂ electrode synthesized using the solution containing Cu-powder is denser than the PbO₂ electrode synthesized with Cu^{2+} ion. The particle size reduction reduces the inner stress of the PbO₂ layer, which thus enhances the stability of the PbO₂ with Cu powder. Finally, this observation displayed that the stabilization of the PbO₂ with Cu-powder because of the dense structure of the layer helps withdraw corrosion of the substrate.

The voltammetric charge (q*) of the anode electrodes was obtained by integrating the voltammetric areas with different scan rates in the 0.1 M HClO₄ solution. The q* parameters incline to reflect the number of electroactive sites on the PbO₂ electrode. A higher q* value indicates
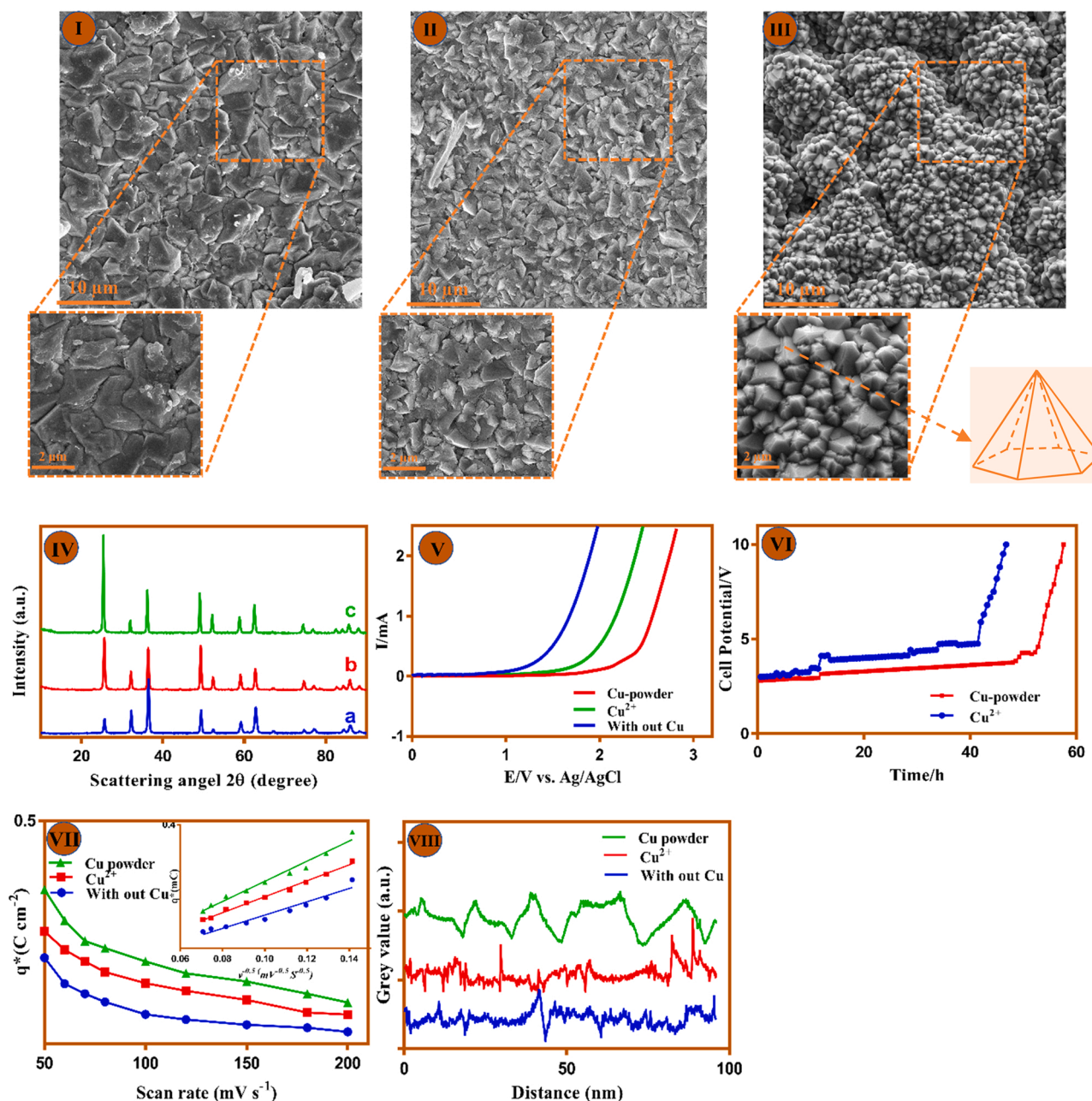
Fig. 1. FESEM images of PbO$_2$ with different sources of Cu in the electrolyte, I) Cu ion-free solution, II) Cu^{2+} ion, and III) Cu-powder. IV) The X-ray diffraction patterns of PbO$_2$ with a different source of Cu in the electrolyte, a) Cu ion-free solution, b) Cu^{2+} ion, and c) Cu-powder. V) the LSVs of PbO$_2$ were obtained at a scan rate of 100 mV s^{-1} in 0.5 M Na$_2$SO$_4$ and pH= 6.0. VI) The accelerated lifetime tests for both PbO$_2$ electrodes in 3.0 M H$_2$SO$_4$ solution at 500 mA cm^{-2}.VII) Voltammetric charge q* at the different scan rates for Cu ion-free solution, Cu^{2+} ion, and Cu-powder electrolyte. The insert shows the q* plot as a function of $v^{-1/2}$. VIII) Gray value intensity for Cu ion-free solution, Cu^{2+} ion, and Cu-powder electrolyte in the same distance.

more significant electrode activity for the same electrode material [35–37]. Calculation method for q* and its parameters are given in supporting information.

Fig. 1 (VII) displays the traditional trends in which q* decreases with increasing scan rates. Here, the Cu-powder PbO$_2$ electrode observes a higher q* than other anode electrodes, but there is no linear relation between the q* with the scan rate. The plot of q* against $v^{-1/2}$ can give better information about the inner capacitance of the anode. The inner capacitance is a robust descriptor for evaluating the number of active sites. The order of the inner capacitance is Cu-powder > Cu^{2+} > PbO$_2$ electrodes. The order shows that Cu-powder PbO$_2$ has more active sites. On the other hand, gray value analysis has been used to prove these results, Fig. 1 (VIII). The sharp corners and transparent edges of PbO$_2$

electrodes were investigated by gray value analysis of FESEM images [38]. The presence of sharp corners and transparent edges causes more compact structures. As shown in Fig. 1 (VIII), Cu-powder PbO$_2$ has sharp edges with good distribution compared to other anode electrodes, representing a more active site in the same range.

XPS analysis as a powerful technique was used to investigate the chemical states and elemental composition of PbO$_2$ electrode in the electrolyte solution containing Cu-powder. The analysis results about the fitting data after the electrodeposition of PbO$_2$ on the anode electrode were summarized in Fig. 2. As shown in Fig. 2 (I), the survey spectrum was calibrated by the C 1 s spectrum at 284.6 (eV). The XPS results show the presence of Pb, O, and Cu elements. The high resolution of the Pb 4 f spectrum shows two strong peaks at binding energies of
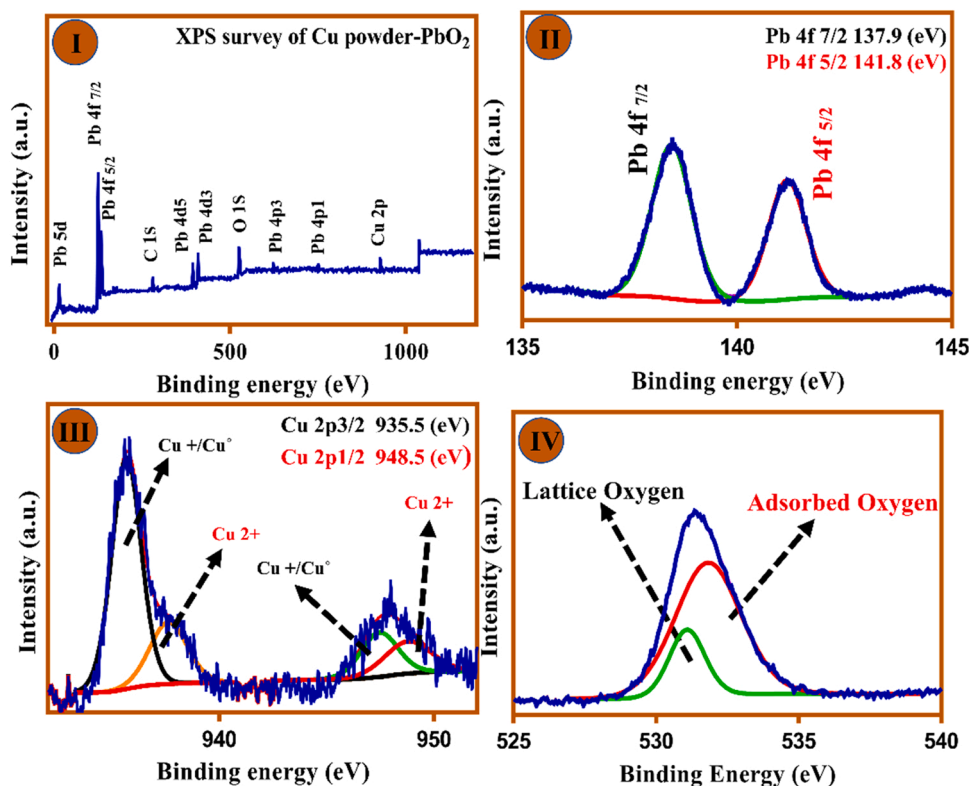
Fig. 2. XPS spectrum of the PbO$_2$ anode. I) XPS fully scanned spectra. II)The high-resolution spectrum of Pb 4f. III) The core level spectrum of Cu 2p. IV) O 1s core level spectrum.

137.9 and 141.8 eV, which correspond to Pb 4 f $_{5/2}$ and Pb 4 f $_{7/2}$ in the β- PbO$_2$, respectively [39,40]. The Cu 2p spectrum consisted of various states of Cu. The Cu 2p $_{3/2}$ and the Cu 2p $_{1/2}$ appeared at around 955.5 and 948.5 (eV), respectively, indicating the Cu embedded into the PbO$_2$ matrix during the electrodeposition process (Fig. 2(III)). The peaks centered at 935.1 and 947.2 (eV) in the Cu 2p spectrum corresponded to Cu$^+$ or metallic Cu. Two characteristic peaks at approximately 936.2 and 949.3 eV can be assigned to the Cu^{2+} state. The presence of Cu ions may be due to the anodic oxidation of Cu powder at the PbO$_2$ electrode or acid dissolution process [41].

The XPS spectra cannot efficiently distinguish metallic Cu or Cu$^+$ due to the peak overlap. The incorporation of Cu ions inside the PbO$_2$ matrix is due to the closeness of the ionic radius of copper to Pb [33,42]. The ionic radius of Cu^{2+} (0.73 ± 0.2 A) is appreciably similar to Pb(VI) (0.77 ± 0.2 A). In the Cu^{2+} ion, the effective nuclear charge is higher leading to the electron being pulled closer to the nucleus, resulting in the decreased radius of Cu^{2+} compared to Cu$^+$. On the other hand, in an aqueous solution, Cu$^+$ ions are not stable, while Cu^{2+} is strongly solvated [43]. As a result, Cu^{2+} and metallic Cu are the dominant species. It is straightforward for Cu^{2+} ions to replace in the PbO$_2$ matrix and form a solid solution with lead dioxide via substitution.

The ICP-AES analysis results verify that the Cu cation embeds in the PbO$_2$ matrix. The ICP-AES analysis results showed that the concentration of Cu ion in the PbO$_2$ matrix was 0.313 mg g^{-1} PbO$_2$. As shown in Fig. 2 (IV), the high-resolution spectrum of O 1 s exhibits two types of active oxygen on the surface of the anode, including the crystal lattice oxygen (O$_L$) and adsorbed/chemisorbed hydroxyl radical (O$_A$). As reported in the literature, the performance of the mineralization process improves with the increase in the O$_A$/O$_L$ ratio [44].

3.2. Characterizations of the cathodic electrodes

Surface morphology and electrochemical activity of the synthesized cathodic electrodes were studied using techniques such as FESEM, and

voltammetry. Fig. 3 (I and II) shows the FESEM images of undoped and ZnO nanoparticles-doped PANI (i.e., PANI@ZnO), respectively. As shown in Fig. 3 (I), the undoped PANI has a plate-like structure. Interestingly, the morphology of PANI@ZnO changes completely to the nanofiber structures in the presence of ZnO nanoparticles as the dopant (Fig. 3 (II)). These results indicate that the morphology of the PANI film strongly depends on the type of dopant. In addition, Fig. 3 (III) shows Pt particles with spherical morphology on the plate-like structure of PANI, demonstrating that Pt particles were successfully deposited on the PANI layer. The FESEM of the Pt deposited on PANI@ZnO (40 mg L^{-1} of ZnO) is shown in Fig. 3 (IV). The FESEM of Pt/PANI@ZnO demonstrates a well-defined cauliflower shape with excellent distribution pores which can be related to the ZnO nanoparticles as a dopant. The cathode electrode of Pt/PANI@ZnO with 40 mg L^{-1} of ZnO nanoparticle demonstrates higher electrochemical activity because of the increased surface area. Fig. 3 (V) presents the cyclic voltammograms of Pt/GP, Pt/PANI/GP, and Pt/ PANI@ZnO (40 mg L^{-1})/GP electrodes tested in 0.1 M H$_2$SO$_4$. The CV curve illustrates that the current densities are largely enhanced due to the increase in surface area. These CV curves clearly show that the electrochemical activity of Pt/ PANI@ZnO (40 mg L^{-1}) was improved.

SFig. (I-III) presents a CV corresponding to the electrochemical characterization of PANI and PANI@ZnO (40 mg L^{-1}) on the GP electrode. The voltammogram curves of the first cycle for PANI and PANI@ZnO (40 mg L^{-1}), are shown in SFig. (I). The first cycle in the PANI electrosynthesis is a nucleation process [45]. The nucleation potential for the electrode shows slightly different values at which each polymer begins to grow. This circumstance is due to an interaction between monomer or oligomer molecules in the solution with ZnO nanoparticles [46]. The 20th cycle of electropolymerization of PANI, shown in SFig. (II), contains well-defined oxidation peaks (E$_{pa1}$ = 0.16 V, E$_{pa2}$ = 0.53 V, and E$_{pa3}$ = 0.79 V vs. Ag/AgCl) in the anodic potential scan. During the cathodic scan, peaks at around E$_{pc1}$= 0.10, E$_{pc2}$= 0.44, and E$_{pc3}$= 0.60 V vs. Ag/AgCl are observed which correspond to several
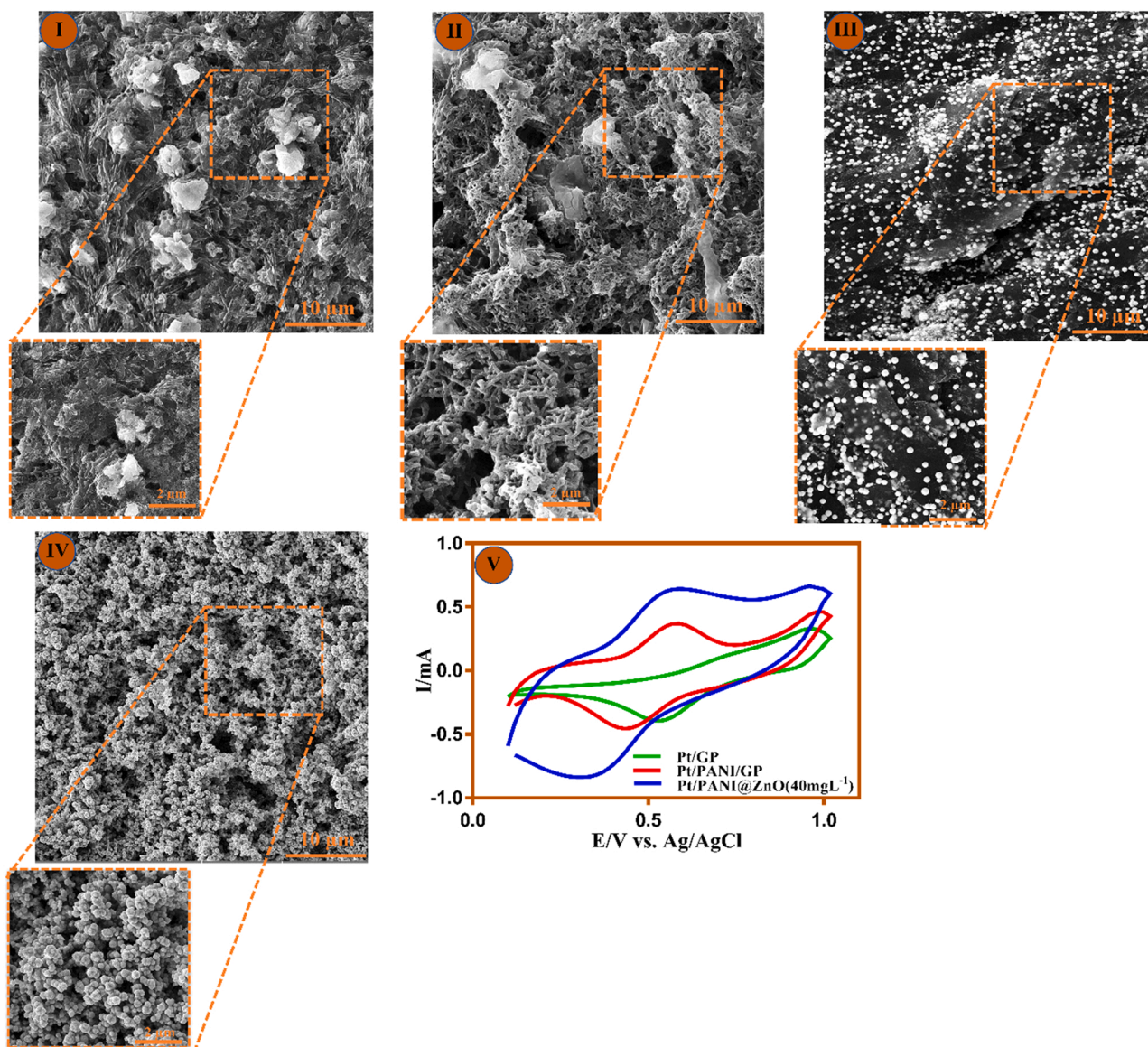
Fig. 3. FESEM images of different cathode materials. I) PANI/GP, II) PANI@ZnO (40mgl^{-1})/GP, III) Pt/PANI/GP, IV) Pt/PANI@ZnO (40 mg L^{-1})/GP. V) CV curves of Pt/GP, Pt/PANI/GP, and Pt/PANI@ZnO (40 mg L^{-1}) in 0.1 M H$_2$SO$_4$.

reduction and oxidation steps of the PANI. In examining the CV of the PANI@ZnO (40 mg L^{-1}), the influence of ZnO nanoparticles in the polymer chain observed has been shown by the decreased current intensity of the redox peaks. The current intensity of the redox peaks can be reduced by the occupied active sites with n-type semiconductors. On the other hand, the decreases in three redox peak potential separations (ΔE = E$_{pc}$-E$_{pa}$) for PANI@ZnO (40 mg L^{-1}) are shown better reversibility/electron transfer rate. This effect has been related to the catalytic effects of ZnO [47]. To characterize, the electrochemical responses of PANI and PANI@ZnO (40 mg L^{-1}) in monomer-free background 0.5 M H$_2$SO$_4$ + 0.01 M LiClO$_4$ solution are displayed and compared together in SFig. (III). The displacement of the potential peaks can be found in the appearance of the position of the reduction and oxidation peaks. ZnO nanoparticles in the backbone of the PANI caused increasing the intensity of the reduction peak for this composite as compared to those for PANI.

The surface elemental analysis of PANI@ZnO (40 mg L^{-1}) composite was chosen based on the evidence from the XPS results. The survey XPS spectrum of PANI@ZnO (40 mg L^{-1}) revealed the coexistence of C, N, O, and Zn on the surface of the cathode electrode. The obtained results from

the fitting process after electrosynthesis of PANI@ZnO (40 mg L^{-1}) were summarized in Fig. 4 (I-V). The appeared peak at binding energies 531.6 and 529.5 (eV) in the O 1 s spectrum corresponded to the O$_A$ and O$_L$ (shown in Fig. 4(II)). The C 1 s peak displays three peaks at 283.8, 284.7, and 285.5 (eV), which can be assigned to (C-H), (C=N), and (C=N +), respectively. As shown in the N core level spectrum, three peaks are displayed, the low energy one may be attributed to quinoid imine (=N$^-$), while the middle and high energy contribute to protonated amine (-N$^+$), and protonated imine (=N$^+$), respectively (Fig. 4 (IV)) [47]. Fig. 4 (V) displays two well-defined and separated peaks centered at 1023.6 and 1041.8 (eV), which can be assigned to Zn 2p3 and Zn 2p1, respectively. These peaks are in agreement with the spectral values for Zn. These results confirmed the presence of ZnO species in the PANI@ZnO (40 mg L^{-1}) composite.

3.3. CO$_2$ electro-reduction

LSV was used to estimate the electrochemical activity of Pt/GP, Pt/PANI/GP, and Pt/PANI@ZnO/GP in 0.5 M KHCO$_3$ (pH = 5.0) under different saturation conditions electrolyte (CO$_2$ and N$_2$) at room
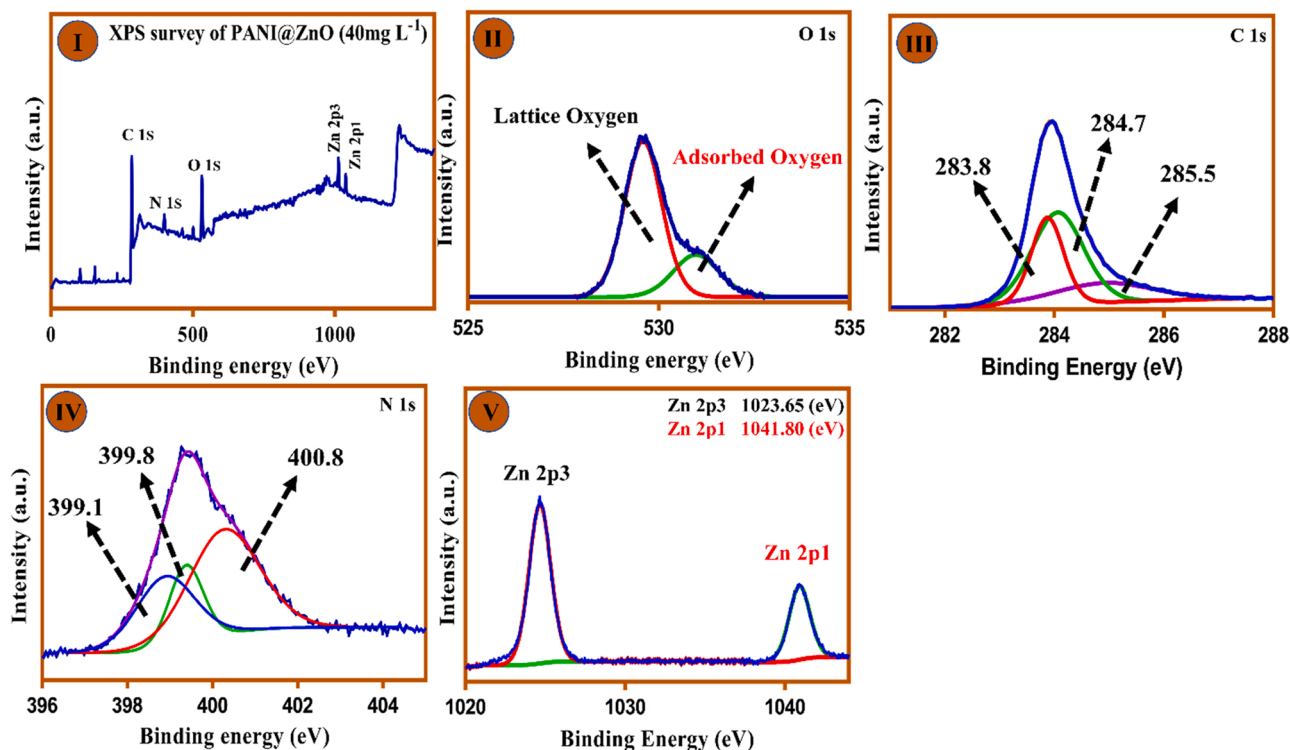
Fig. 4. I)XPS spectrum of the PANI@ZnO cathode. The core level spectrum for PANI@ZnO II) O 1s, III) C 1s, IV) N 1s and V) Zn 2p.
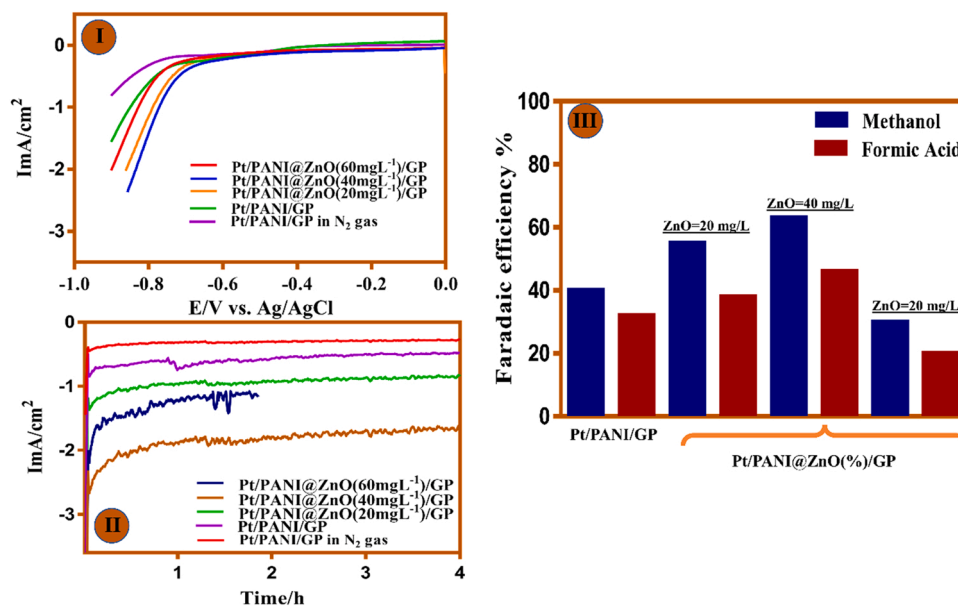

Fig. 5. I) LSV curves of different cathode materials obtained in the 0.5 M Na_2SO_4 electrolyte saturated by N_2 and CO_2. II) Current densities of different cathode materials in 0.5 M Na_2SO_4 during 4 h electrolysis at constant potential (-0.8 V) in electrolyte saturated by N_2 and CO_2. III) Product distributions of CO_2 reduction in the different electrode materials.

temperature. Fig. 5 (I) demonstrates the obtained LSV curves at different electrodes. As it is obvious, the current densities of the electrodes in the CO_2 saturation condition are much higher compared to the saturation of N_2. The peak potential for the reduction reaction obtained for the CO_2 saturated electrolyte was less negative than that for the N_2 saturated electrolyte. Numerous reports have shown the different performances of PANI highlighting the importance of the functional groups and structure for electrocatalyst applications. The performance of PANI for CO_2 reduction can be improved by the use of different loading amounts of

ZnO. Thereby, by changing the loading percent of the ZnO nanoparticles, it is possible to change the resulting reduction process by creating a new active site. Among them Pt/PANI@ZnO (40 mg L^{-1})/GP shows slightly fewer negative potentials and the highest current density, indicating that Pt/PANI@ZnO (40 mg L^{-1})/GP has a high-performance activity for CO_2 reduction.

Both hydrogen evolution reaction (HER) and CO_2 reduction occur in the same range of potential. Thereby, the current associated with CO_2 reduction can be hindered by HER, which occurs at a faster rate, as the

current observed for this cell can be attributed to each reaction. Based on LSV plots, the improved selectivity toward CO_2 reduction cannot be verified. To understand the catalytic activity of the Pt/PANI@ZnO electrodes, potentiostatic bulk electrolysis was carried out at the potential of -0.8 V against Ag/AgCl as an indication of the conversion efficiency. The catholyte solution was analyzed using gas chromatography (GC) methods.

Fig. 5 (II) presents the controlled potential electrolysis at the different electrodes with the same electrolyte composition. As evident, the reduction current was increased to $2\,mA\,cm^{-2}$, for the Pt/PAN-I@ZnO (40 mg L^{-1})/GP electrode. The current density was unchanged during the 4 h of electrolysis indicating the stability of the Pt/PAN-I@ZnO (40 mg L^{-1})/GP catalyst in this time window. However, higher loading ZnO nanoparticle levels may decrease the electrical conductivity of the PANI electrodes. The percentage of ZnO nanoparticles exceeds 60 mg L^{-1}, which causes the stability of the electrode to decrease due to the structure collapse as shown in Fig. 5 (II).

The faradaic efficiency (FE) for the non-paired system was calculated by the equation given in STable 1 and also plotted in Fig. 5 (III). Formic acid and methanol were detected in the catholyte that was produced during the electrolysis. Optimized Pt/PANI@ZnO (40 mg L^{-1})/GP demonstrated significantly higher FEs for methanol (63%) and formic acid (46%) than either other composition also formed. This catalyst has a high adsorption capacity toward CO intermediate adsorption. It can be adsorbed at the surfaces of PANI@ZnO through hydrogen bonding interactions with the NH_2- group of PANI. On the other hand, ZnO is an amphoteric oxide and has good capability to absorb CO intermediate. It can help to produce methanol and formic acid, which require more electron transfer.

3.4. Electrochemical behavior of AMD 10B

To the best of our knowledge, the electrochemical behavior of AMD 10B in aqueous solutions has not been reported to this date. In the first step, the electrochemical behavior of AMD 10B was investigated by CV at different switching potentials and scanning directions by comparing the first and second cycles. The CVs of AMD10B change with the potential sweep at a wide range from -0.9–1.3 V vs Ag/AgCl. The different direction scanning of potential can be observed in Fig. 6 (I-IV). The electrode potential was scanned in different switching potentials.
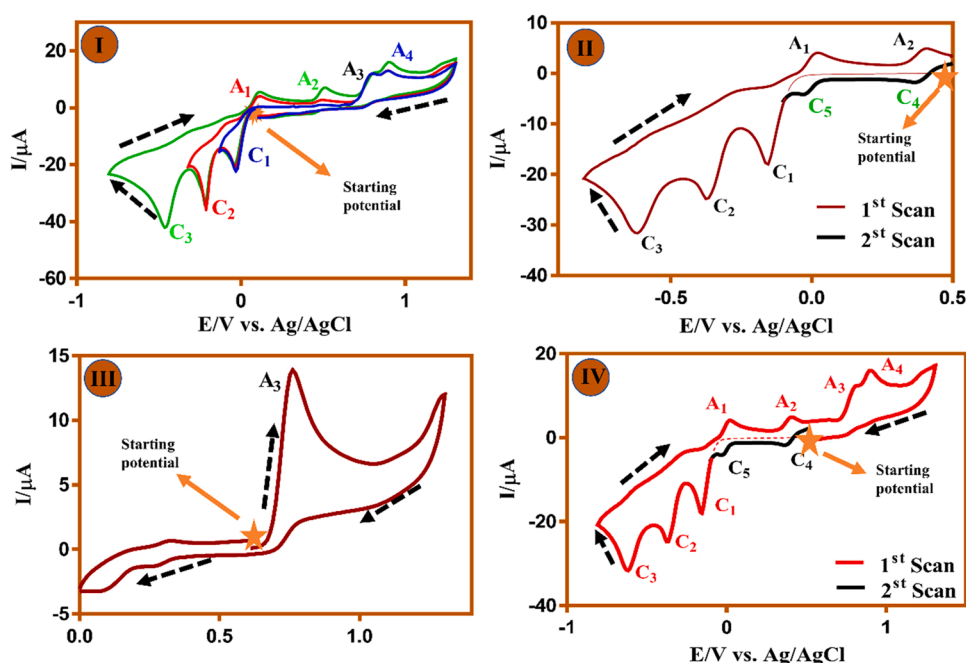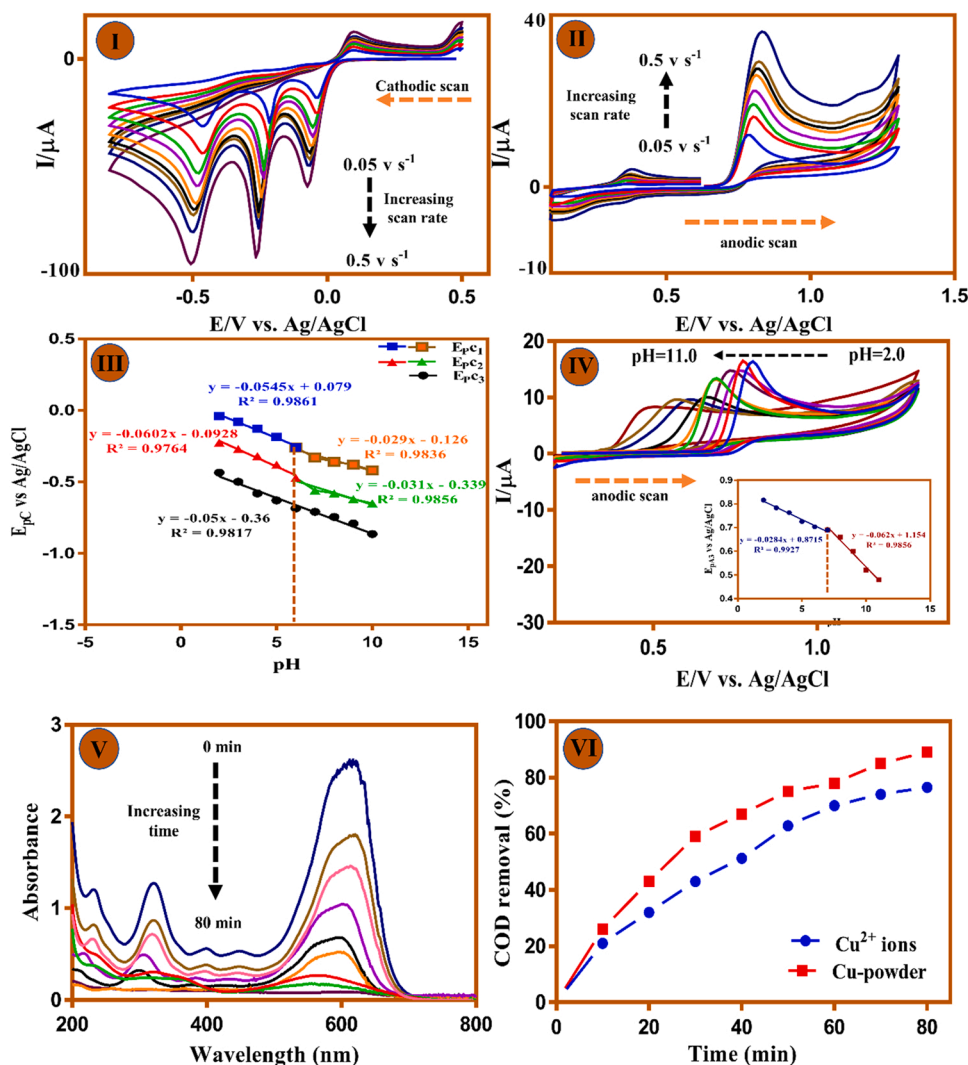
The CVs exhibit three irreversible cathodic peaks C_1, C_2, and C_3 in the cathodic direction scan, as shown in Fig. 6 (I). The observed cathodic peaks correspond to the reduction of two azo bonds and a nitro group in AMD 10B molecule. Additionally, Fig. 6 (I) shows that the cathodic peaks are independent of each other. Conversely, in the anodic direction scan four anodic peaks A_1, A_2, A_3, and A_4 were observed in the four different potential values. Under these conditions, new anodic peaks C_4 and C_5 attributed to the new electroactive intermediates appear in two consecutive potential scans from $+0.5$ to -0.85 V vs. Ag/AgCl, as shown in Fig. 6 (II). These cathodic peaks correspond to the reversible counterpart for anodic peaks A_1 and A_2. During a positive-going scan, the CV presents the large irreversible anodic peak A_3 at near $+0.8$ V (Fig. 6 (III)). The anodic peak A_3 attributed to the oxidation state of AMD 10B to its intermediate and presumably degraded into nitroso benzene and 1-nitro-4-nitroso benzene with the intervention of water [48]. The C_1 peak is slightly more positive than another cathodic peak because the NO_2 group is located near the azo bound. The peak C_1 belongs to the reduction of AMD 10B into reduction form (AMD $10B_{red1}$), then generated *para*-nitroaniline and A_4 peak corresponded to the oxidation of cathodically generated intermediate. The radical intermediate formed during the oxidation of the NH_2-group in *para*-nitroaniline is destabilized when the strong electro-withdrawing NO_2-group is located in the *para* position. This is due to the fact that the form causes the electro-oxidation process of the amine group to occur in more positive potentials [49]. The peak C_2 is attributed to the reduction of AMD $10B_{red1}$ to AMD $10B_{red2}$, and the A_1 peak belongs to the oxidation of cathodically degraded then generated A_1/C_5 reversible couple (presumably the radical cation of aniline) [50,51]. Under these circumstances, the cathodic peak C_3 corresponded to the reduction of the nitro group in AMD $10B_{red2}$ and generated phenylhydroxylamine leading to the A_2/C_4 reversible couple [52]. As shown in Fig. 6 (IV), the CV curves of AMD 10B at a wide-range window were scanned and compared with the first and second cycles. In this curve, all redox peaks and the couple that was examined above are clearly visible.

In order to investigate the electrochemical behavior of AMD 10B, the CV curves at various scan rates in cathodic and anodic directions were studied. The first point that can be discovered in this part, the intensity of cathodic peaks of I_{PC1} I_{PC2}, and I_{PC3} are enhanced with increasing potential scan rates. Also, the anodic peak intensity of I_{pA3} increases by increasing potential scan rates (Fig. 7 (II)). In addition, the diffusion-

Fig. 6. I) CV curves of AMD 10B 0.3 M in aqueous phosphate buffer solution (c= 0.2 M, pH=2.0) with different switching potentials ($+0.4$ to -0.13, -0.32, and -0.8, then to $+1.3$ V vs. Ag/AgCl)) on the glassy electrode. II) The CV curves obtained from the first and second cycles from $+0.5$ to -0.85 in the same electrolyte solution. III) The CV of AMD 10B in aqueous solution in a positive-going scan with three potential switchings ($+0.6$–1.3 and then 0 V vs. Ag/AgCl), IV) The electrochemical behavior of AMD 10B obtained from first and second cycles at wide range potential from $+1.3$ to -0.85 V vs. Ag/AgCl).

Fig. 7. I-II) CVs of AMD 10B 0.1 M in an aqueous phosphate buffer solution (pH=2.0 and c=0.2 M) with different scan rates (0.05 V s^{-1} to 0.5 V s^{-1}) on the glassy electrode for the cathodic and anodic direction. III) The E-pH diagram for cathodic direction. IV) The anodic scan for AMD 10B 0.1 M in aqueous solution with different pH values, pHs are 2.0, 3.0, 4.0, 5.0, 6.0, 7.0, 8.0, 9.0, and 10.0) and E-pH diagram for anodic direction. V) UV–Vis absorption spectra of AMD 10B 0.1 M, during bulk electrolysis at 15 mA cm^{-2} using Cu-powder anode in two-compartment cells. VI) IV) COD removal efficiency at the pH = 7.0 for AMD 10 0.1 M for Cu^{2+} and Cu-powder PbO$_2$ electrode at 15 mA cm^{-2}.

adsorption behavior of redox AMD 10B was shown in SFigs. (IV-VI). The I_{pC1}, I_{pC2}, I_{pC3}, and I_{pA3} at different scan rates show a good linear relationship with the $v^{1/2}$, and the corresponding equation can be expressed as y = −72.253x + 0.382 (R^2 = 0.994), y = −110.63x - 1.466 (R^2 = 0.993), y = −109.04x - 3.736 (R^2 = 0.989), and y = 50.759x - 0.083 (R^2 = 0.997), respectively. This observation displays that the electrode reaction of AMD 10B is a diffusion-controlled process. Also, the logarithm of redox peak currents (log I_{pC1}, I_{pC2}, I_{pC3}, and I_{pA3}) was plotted against the log v for AMD 10B oxidation. The obtained slope value is very close to the theoretical value of 0.5. It was previously published that when the slope is nearly close to 0.50, the electrochemical reaction is a diffusion-controlled process [53].

The electrochemical oxidation/reduction process of AMD 10B in various pHs was also studied. The results are shown in Fig. 7 (III and IV) and SFig. (VII). As can be seen, E_{pA3} is slightly shifted to a less positive potential with an increase in pH, and a similar behavior for oxidation of azo bound is observed in the recently reported research work [47]. The cathodic peak potentials shifted linearly toward less positive values with increasing the pH from 2 to 10. The obtained results demonstrate the participation of proton in the electro-oxidation of AMD 10B. In the acidic pH, the protonated AMD 10B is the dominant species, and its oxidation potential is more negative compared to the AMD 10B. The diagram of E_{pA3} with pH comprises two linear segments with different slopes of − 28 mV/pH and − 62 mV/pH, indicating that at pH ≤ 6 the AMD 10B oxidation is a two-electron/one-proton process. This result

approves the oxidation of AMD 10B to oxidation intermediate. Finally, at pH ≥ 6, the oxidation reaction probably includes a two-electron/two-proton process. Moreover, the plot of E (E_{pc1}, and E_{pc2})-pH shows two linear segments with different slopes of − 54 mV/pH, − 29 mV/pH (for E_{pc1}), and − 60 mV/pH, − 31 mV/pH (for E_{pc2}). The E_{pc1} and E_{pc2} values are dependent on pH, indicating that the cathodic peaks involve the same electron and proton numbers (2 electron /2 protons or 4 electron /4 protons) process for the reduction reaction at a pH lower than 6.0. According to the observations, it can be suggested that the reduction process at a pH lower than 6 can occur in two pathways. The first pathway is the direct reduction of AMD 10B to the AMD 10B$_{red1-3}$ intermediates. In the second pathway, the water intervention of AMD 10B reduces in a 4 electrons/4 protons process. From the obtained results it can be concluded that the second pathway takes place. Then at pH ≥ 6 peak potential shifts indicate the reduction reaction is a two-electrons/one proton process. In the E_{pc3}-pH plot, the potential value E_{pc3} shifted by − 50 mV/pH. The condition of the process is a little complicated. This shift indicates the reduction process probably is four electrons/four protons process.

The oxidative degradation progress in a two-compartment cell at a current density of 15 mA cm^{-2} was also monitored by using a UV–Vis spectrophotometry. Fig. 7 (V) shows the results. The UV–Vis spectrum of AMD 10B shows two absorbance peaks in the UV region at 226 and 318 nm and one peak in the visible region at 617 nm. The obtained results indicated that the absorbance spectrum of AMD 10B decreases

and then disappeared completely after 80 min. A new peak was not observed during the degradation of AMD 10B, which indicated that during the degradation process, no stable UV–Vis active intermediate is produced. The higher degradation efficiency and COD removal efficiency for the Cu-powder PbO$_2$ electrode can be related to the synthesis situation shown in Fig. 7 (VI). The high crystallization and compact surface significantly increase the surface area, leading to an increase in the number of sites for the production of an in-situ generation of nonselective powerful oxidizing agents such as Cl$_2$ and OH$^.$, which is useful for oxidation treatment. The proposed electrochemical pathway of AMD 10B was confirmed by the above studies which corresponded to several intermediate compounds formed during the degeneration process as shown in Scheme 2.

3.5. Electro-oxidation of AMD 10B pairing with CO$_2$ electro-reduction

For the next step, the simultaneous processes of reduction/oxidation were conducted under galvanostatic mode at different current densities (10, 15, and 20 mA cm^{-2}) for 4 h with a two-compartment cell separated by a Nafion membrane. The performance of the process can be improved by the application of the optimum current density. The cathodic process was performed in an aqueous solution consisting of 0.5 M Na$_2$SO$_4$ at pH 5.0 and saturated with CO$_2$ at room temperature. While the anolyte consisted of 0.5 M Na$_2$SO$_4$ at pH 5.0 in an aqueous solution that contained AMD 10B (0.1 M) as an electro-oxidation reactant over PbO$_2$.

The sampling taken from catholyte and anolyte during the electrochemical process was performed per 2 h and analyzed by GC and COD methods. Fig. 8 (I) shows the FE of CO$_2$ electro-reduction paired with electro-oxidation of AMD 10B at different current densities. The last yellow column plotted in Fig. 8 (I) presented COD removal based on the monitored anolyte. As expected, the FE of the paired system decreased slightly compared to the nonpaired system, which indicates that the IR drop in the paired system is increased because of presumably blocking the separator with dye or the OER reaction easier run compared with the generation of reactive oxidant species. As evident, at 10 mA cm^{-2} when time increased, the formic acid produced a slow but continuous over time while the methanol continued at a faster rate was observed. The

possible reaction pathway reported in the recent papers showed the first step of methanol and formic acid production is formate ion (HCOO$^-$) forming. PANI@ZnO can hinder the HER and strong adsorption of the HCOO$^-$ so that most of the electron supplied is consumed in methanol production. In parallel, in the anodic compartment, after 4 h electro-oxidation of AMD 10B, the COD removal efficiency of 72% was achieved.

Electrolysis at 15 mA cm^{-2} obtained a slight improvement in the yield of the formic acid (41% FE) but the percentage of methanol significantly increased (57% FE). In the anodic compartment with increased current density, the oxidation process was very rapid, and COD removal efficiency (83%) was achieved. Since the current at 20 mA cm^{-2} was applied, the FE of reduction products decreased due to the HER competitive reaction. Thereby, applying the 15 mA cm^{-2} is feasible to improve the total FE and hence increase the performance of the coupled electrochemical process.

The anode potential was measured between the anode and Ag/AgCl electrode situated close to the anode. Also, the same measurement conditions were applied to the cathode potential. As shown in Fig. 8 (II), The anode potential (OER) was slightly increased between 1.21 and 1.42 V vs. Ag/AgCl, and the cathode potential was increased with a low slope between −0.81 to −1.2 V vs. Ag/AgCl with increasing the current density in the non-paired system. The calculated overall cell voltage for the non-paired system at 15 mA cm^{-2} is 2.66 V vs. Ag/AgCl; also, in the measured overall cell voltage (a multimeter was connected between the cathode and anode), a resistive loss appeared. The measured overall voltage cell at 15 mA cm^{-2} is 3.12 V vs. Ag/AgCl (shown in Fig. 8 (III)). The appeared resistance (ca. 0.46 V was detected) was related to the solution resistance (R$_s$) and membrane resistance (R$_m$). Optimization geometry of the cell and distance between electrodes can reduce the resistance.

For the paired system increase in anode potential is the significant problem that leads to the higher cell voltage. To overcome this challenge, NaCl was used in the anolyte. As can be seen in STable 1, the half-reactions and standard electrode potential of the non-paired and paired system are provided. When using NaCl in anolyte, the cell potential increases by only about 0.8 V during 4 h of the electrolysis process. This potential change is not significant for a paired system with the
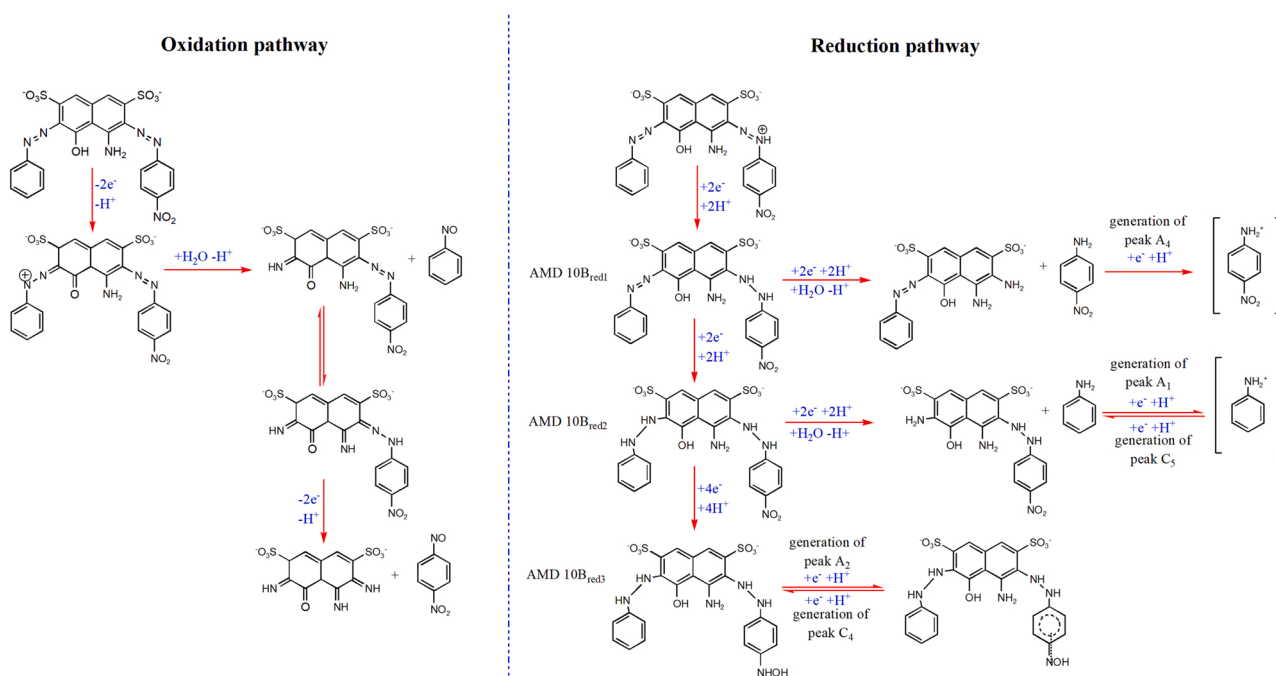
Scheme 2. Probable oxidation/ reduction mechanism for AMD 10B in acidic media.
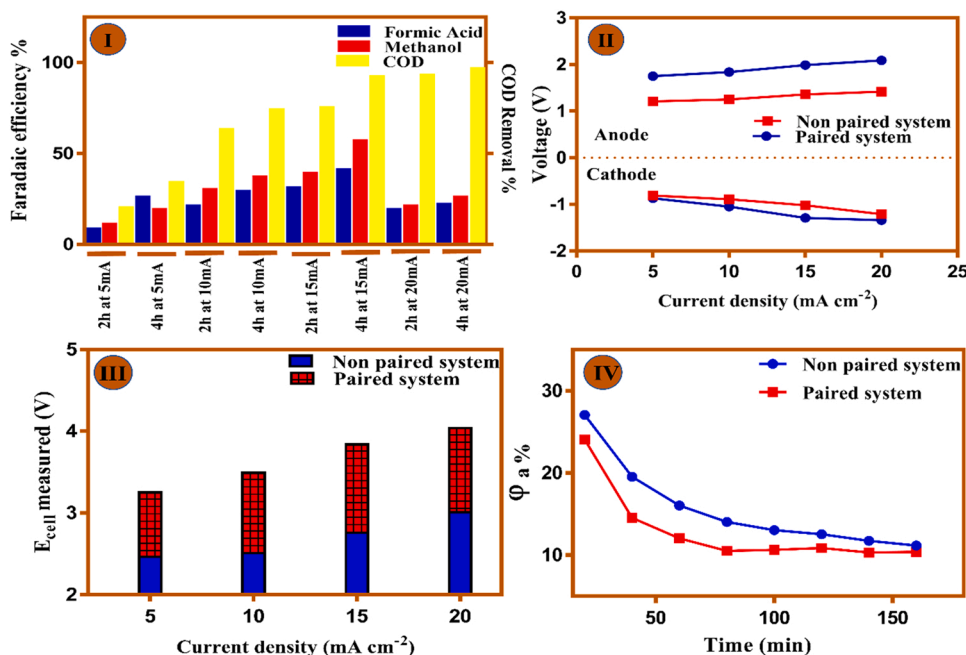
Fig. 8. I) The FE and COD removal efficiency of the paired system at Pt/PANI@ZnO (40 mg L^{-1}) as cathode and Cu-powder PbO$_2$ electrode as anode with different current densities (10, 15, and 20 mA cm^{-2}), sampling during 2 h and 4 h electrolysis. II) Average potentials and III) average cell voltage during the non-paired and paired electrolysis system for the single anode and cathode electrodes at different current densities (5,10, 15, and 20 mA cm^{-2}) during 4 h electrolysis. IV) Current efficiency as a function of electrolysis time for electrochemical oxidation of AMD 0.1 M 10B in presence of 0.5 M NaCl for non-paired and paired electrolysis systems at the current density of 15 mA cm^{-2} during 4 h electrolysis.

simultaneous production of the products in two compartments (shown in Fig. 8 (III)).

In addition, an anodic current efficiency with the electrolysis time was plotted to find the effect of the paired system on anodic current efficiency (Fig. 8(IV)). As it is evident, the current efficiency for a non-paired system decreases with the increase in electrolysis time, and the same behavior can be seen in the paired system. Degradation of AMD 10B in the paired system causes a slight drop in the current efficiency and therefore an increase in power consumption. More comparative parameters for paired and non-paired systems are available in STable 2.

4. Conclusion

The CO$_2$ electro-reduction convert to value products paired with the electro-degeneration of AMD 10B has been experimentally introduced. By this approach, using the electron in both compartments allows the reach of the maximum total FE and reduces energy consumption. As evident, the paired process can significantly improve the techno-economic evaluation of CO$_2$ electro-reduction. Our results show the production of valuable products obtained from both electrochemical compartments. Even though CO$_2$ reduction might ultimately become an economically feasible system. The electrocatalytic effect of Pt/PANI@ZnO (40 mg L^{-1}) was tested for the cathodic compartment to the conversion of a hazardous pollutant to valuable products in the aqueous media. The FE for methanol and formic acid production and total cathodic energy efficiency were 57%, 41%, and 34%, respectively, for the 4 h durability test at cathodic potential − 1.09 V vs Ag/AgCl. Simultaneously for the β-PbO$_2$ electrode the COD removal reached up to 93% with specific energy consumption of 4.6 kWh m^{-3}. Finally, the composition and morphology of such catalysts are characterized. The β-PbO$_2$ layer electrodeposition was synthesized on the anodic electrode into the anolyte containing 300 mg L^{-1} Cu powder. The proposed method presents a high overpotential for OER, high stability of electrode (the longest service life 56 h), and high volume/surface area of the β-PbO$_2$. Another noteworthy point in this paper is to propose and describe an electrochemical behavior for AMD 10B.

CRediT authorship contribution statement

Sina Khalili: Conceptualization, Methodology, Investigation,

Writing – original draft. **Abbas Afkhami:** Supervision, Conceptualization, Writing – review & editing, Critically revised the manuscript. **Tayyebeh Madrakian:** Supervision, Writing – review & editing.

Declaration of Competing Interest

The authors declare that they have no known competing financial interests or personal relationships that could have appeared to influence the work reported in this paper.

Data availability

No data was used for the research described in the article.

Appendix A. Supplementary material

Supplementary data associated with this article can be found in the online version at doi:10.1016/j.apcatb.2023.122545.

References

[1] P. Friedlingstein, M.W. Jones, M. O'Sullivan, R.M. Andrew, D.C. Bakker, J. Hauck, C. Le Quéré, G.P. Peters, W. Peters, J. Pongratz, Global carbon budget 2021, Earth Syst. Sci. Data 14 (2022) 1917–2005, https://doi.org/10.5194/essd-14-1917-2022.

[2] J. Albo, M. Alvarez-Guerra, P. Castaño, A. Irabien, Towards the electrochemical conversion of carbon dioxide into methanol, Green Chem. 17 (2015) 2304–2324, https://doi.org/10.1039/C4GC02453B3.

[3] S.C. Roy, O.K. Varghese, M. Paulose, C.A. Grimes, Toward solar fuels: photocatalytic conversion of carbon dioxide to hydrocarbons, ACS Nano 4 (2010) 1259–1278, https://doi.org/10.1021/nn9015423.

[4] G. Fiorani, W. Guo, A.W. Kleij, Sustainable conversion of carbon dioxide: the advent of organocatalysis, Green Chem. 17 (2015) 1375–1389, https://doi.org/10.1039/C4GC01959.

[5] X.-F. Liu, K. Zhang, L. Tao, X.-B. Lu, W.-Z. Zhang, Recent advances in electrochemical carboxylation reactions using carbon dioxide, Green Chem. Eng. (2021), https://doi.org/10.1016/j.gce.2021.12.001.

[6] J. Zhu, W. Zhang, Y. Li, W. Yue, G. Geng, B. Yu, Enhancing CO$_2$ catalytic activation and direct electroreduction on in-situ exsolved Fe/MnOx nanoparticles from (Pr, Ba) 2Mn2-yFeyO5+ δ layered perovskites for SOEC cathodes, Appl. Catal. B Environ. 268 (2020), 118389, https://doi.org/10.1016/j.apcatb.2019.118389.

[7] S. Dongare, N. Singh, H. Bhunia, P.K. Bajpai, A.K. Das, Electrochemical reduction of carbon dioxide to ethanol: a review, ChemistrySelect 6 (2021) 11603–11629, https://doi.org/10.1002/slct.202102829.

[8] Y. Jiang, F. Chen, C. Xia, A review on cathode processes and materials for electro-reduction of carbon dioxide in solid oxide electrolysis cells, J. Power Sources 493 (2021), 229713, https://doi.org/10.1016/j.jpowsour.2021.229713.

[9] W. Deng, T. Yuan, S. Chen, H. Li, C. Hu, H. Dong, B. Wu, T. Wang, J. Li, G.A. Ozin, Effect of bicarbonate on CO_2 electroreduction over cathode catalysts, Fundam. Res. 1 (2021) 432–438, https://doi.org/10.1016/j.fmre.2021.06.004.

[10] S.A. Al-Tamreh, M.H. Ibrahim, M.H. El-Naas, J. Vaes, D. Pant, A. Benamor, A. Amhamed, Electroreduction of carbon dioxide into formate: a comprehensive review, ChemElectroChem 8 (2021) 3207–3220, https://doi.org/10.1002/celc.202100438.

[11] H. Jiang, Y. Zhao, L. Wang, Y. Kong, F. Li, P. Li, Electrochemical CO_2 reduction to formate on tin cathode: influence of anode materials, J. CO_2 Util. 26 (2018) 408–414, https://doi.org/10.1016/j.jcou.2018.05.029.

[12] A.V. Rudnev, U.E. Zhumaev, A. Kuzume, S. Vesztergom, J. Furrer, P. Broekmann, T. Wandlowski, The promoting effect of water on the electroreduction of CO_2 in acetonitrile, Electrochim. Acta 189 (2016) 38–44, https://doi.org/10.1016/j.electacta.2015.12.088.

[13] Y. Zhong, Y. Xu, J. Ma, C. Wang, S. Sheng, C. Cheng, M. Li, L. Han, L. Zhou, Z. Cai, An artificial electrode/electrolyte interface for CO_2 electroreduction by cation surfactant self-assembly, Angew. Chem. 132 (2020) 19257–19263, https://doi.org/10.1002/ange.202005522.

[14] P. Moreno-García, Nm Kovács, V. Grozovski, M.a.d.J.s. Gálvez-Vázquez, S. Vesztergom, P. Broekmann, Toward CO_2 electroreduction under controlled mass flow conditions: a combined inverted RDE and gas chromatography approach, Anal. Chem. 92 (2020) 4301–4308, https://doi.org/10.1021/acs.analchem.9b04999.

[15] S. Liang, N. Altaf, L. Huang, Y. Gao, Q. Wang, Electrolytic cell design for electrochemical CO_2 reduction, J. CO_2 Util. 35 (2020) 90–105, https://doi.org/10.1016/j.jcou.2019.09.007.

[16] B. Wei, Y. Xiong, Z. Zhang, J. Hao, L. Li, W. Shi, Efficient electrocatalytic reduction of CO_2 to HCOOH by bimetallic In-Cu nanoparticles with controlled growth facet, Appl. Catal. B Environ. 283 (2021), 119646, https://doi.org/10.1016/j.apcatb.2020.119646.

[17] H. Han, S. Jin, S. Park, M.H. Seo, W.B. Kim, Atomic iridium species anchored on porous carbon network support: an outstanding electrocatalyst for CO_2 conversion to CO, Appl. Catal. B Environ. 292 (2021), 120173, https://doi.org/10.1016/j.apcatb.2021.120173.

[18] Y. Liu, F. Li, X. Zhang, X. Ji, Recent progress on electrochemical reduction of CO_2 to methanol, Curr. Opin. Green Sustain. Chem. 23 (2020) 10–17, https://doi.org/10.1016/j.cogsc.2020.03.009.

[19] E. Pérez-Gallent, S. Turk, R. Latsuzbaia, R. Bhardwaj, A. Anastasopol, F. Sastre-Calabuig, A.C. Garcia, E. Giling, E. Goetheer, Electroreduction of CO_2 to CO paired with 1, 2-propanediol oxidation to lactic acid. Toward an economically feasible system, Ind. Eng. Chem. Res. 58 (2019) 6195–6202, https://doi.org/10.1021/acs.iecr.8b06340.

[20] M. Abdinejad, C. Ferrag, M.N. Hossain, M. Noroozifar, K. Kerman, H.B. Kraatz, Capture and electroreduction of CO2 using highly efficient bimetallic Pd–Ag aerogels paired with carbon nanotubes, J. Mater. Chem. A 9 (2021) 12870–12877, https://doi.org/10.1039/D1TA01834E.

[21] X.V. Medvedeva, J.J. Medvedev, S.W. Tatarchuk, R.M. Choueiri, A. Klinkova, Sustainable at both ends: electrochemical CO 2 utilization paired with electrochemical treatment of nitrogenous waste, Green Chem. 22 (2020) 4456–4462, https://doi.org/10.1039/D0GC01754J.

[22] S. Sabatino, A. Galia, G. Saracco, O. Scialdone, Development of an electrochemical process for the simultaneous treatment of wastewater and the conversion of carbon dioxide to higher value products, ChemElectroChem 4 (2017) 150–159, https://doi.org/10.1002/celc.201600475.

[23] T. Li, Y. Cao, J. He, C.P. Berlinguette, Electrolytic CO_2 reduction in tandem with oxidative organic chemistry, ACS Cent. Sci. 3 (2017) 778–783, https://doi.org/10.1021/acscentsci.7b00207.

[24] A.N. Grace, S.Y. Choi, M. Vinoba, M. Bhagiyalakshmi, D.H. Chu, Y. Yoon, S. C. Nam, S.K. Jeong, Electrochemical reduction of carbon dioxide at low overpotential on a polyaniline/Cu2O nanocomposite based electrode, Appl. Energy 120 (2014) 85–94, https://doi.org/10.1016/j.apenergy.2014.01.022.

[25] R. Aydin, F. Köleli, Electrochemical reduction of CO_2 on a polyaniline electrode under ambient conditions and at high pressure in methanol, J. Electroanal. Chem. 535 (2002) 107–112, https://doi.org/10.1016/S0022-0728(02)01151-8.

[26] W. Zheng, S. Nayak, W. Yuan, Z. Zeng, X. Hong, K.A. Vincent, S.C.E. Tsang, A tunable metal–polyaniline interface for efficient carbon dioxide electro-reduction to formic acid and methanol in aqueous solution, Chem. Commun. 52 (2016) 13901–13904, https://doi.org/10.1039/C6CC07212G.

[27] V. Eskizeybek, F. Sarı, H. Gülce, A. Gülce, A. Avcı, Preparation of the new polyaniline/ZnO nanocomposite and its photocatalytic activity for degradation of methylene blue and malachite green dyes under UV and natural sun lights irradiations, Appl. Catal. B Environ. 119 (2012) 197–206, https://doi.org/10.1016/j.apcatb.2012.02.034.

[28] J. Arjomandi, S. Tadayyonfar, Electrochemical synthesis and in situ spectroelectrochemistry of conducting polymer nanocomposites. I. polyaniline/TiO2, polyaniline/ZnO, and polyaniline/TiO2+ ZnO, Polym. Compos. 35 (2014) 351–363, https://doi.org/10.1002/pc.22870.

[29] T.C. Wen, M.G. Wei, K.L. Lin, Electrocrystallization of PbO2 deposits in the presence of additives, J. Electrochem. Soc. 137 (1990) 2700, https://doi.org/10.1149/1.2087017.

[30] O. Shmychkova, T. Luk'Yanenko, A. Velichenko, L. Meda, R. Amadelli, Bi-doped PbO2 anodes: electrodeposition and physico-chemical properties, Electrochim. Acta 111 (2013) 332–338, https://doi.org/10.1016/j.electacta.2013.08.082.

[31] O. Shmychkova, T. Luk'Yanenko, R. Amadelli, A. Velichenko, Electrodeposition of Ce-doped PbO2, J. Electroanal. Chem. 706 (2013) 86–92, https://doi.org/10.1016/j.jelechem.2013.08.002.

[32] T. Luk'Yanenko, O. Shmychkova, A. Velichenko, PbO2-surfactant composites: electrosynthesis and catalytic activity, J. Solid State Electrochem. 24 (2020) 1045–1056, https://doi.org/10.1007/s10008-020-04572-8.

[33] X. Hao, S. Dan, Z. Qian, Y. Honghui, W. Yan, Preparation and characterization of PbO 2 electrodes from electro-deposition solutions with different copper concentration, RSC Adv. 4 (2014) 25011–25017, https://doi.org/10.1039/C4RA03235G.

[34] L. Wu, C. Zhang, Y. Sun, Y. Wang, B. Lian, Y. Chen, Y. Tu, T.D. Waite, Cu-mediated optimization of PbO2 anodes for electrochemical treatment of electroless nickel plating wastewater, Chem. Eng. J. 450 (2022) 138188, https://doi.org/10.1016/j.cej.2022.138188.

[35] S. Ardizzone, G. Fregonara, S. Trasatti, "Inner" and "outer" active surface of RuO2 electrodes, Electrochim. Acta 35 (1990) 263–267, https://doi.org/10.1016/0013-4686(90)85068-X.

[36] G. Hua, X. Zhicheng, Q. Dan, W. Dan, X. Hao, Y. Wei, J. Xiaoliang, Fabrication and characterization of porous titanium-based PbO2 electrode through the pulse electrodeposition method: deposition condition optimization by orthogonal experiment, Chemosphere 261 (2020) 128157, https://doi.org/10.1016/j.chemosphere.2020.128157.

[37] C. Rozain, E. Mayousse, N. Guillet, P. Millet, Influence of iridium oxide loadings on the performance of PEM water electrolysis cells: part I–pure IrO2-based anodes, Appl. Catal. B Environ. 182 (2016) 153–160, https://doi.org/10.1016/j.apcatb.2015.09.013.

[38] R. Gheitaran, A. Afkhami, T. Madrakian, Effect of light at different wavelengths on polyol synthesis of silver nanocubes, Sci. Rep. 12 (2022) 19202, https://doi.org/10.1038/s41598-022-23959-3.

[39] S. Chai, G. Zhao, Y. Wang, Y.-n Zhang, Y. Wang, Y. Jin, X. Huang, Fabrication and enhanced electrocatalytic activity of 3D highly ordered macroporous PbO2 electrode for recalcitrant pollutant incineration, Appl. Catal. B Environ. 147 (2014) 275–286, https://doi.org/10.1016/j.apcatb.2013.08.046.

[40] W. Wang, X. Duan, X. Sui, Q. Wang, F. Xu, L. Chang, Surface characterization and electrochemical properties of PbO2/SnO2 composite anodes for electrocatalytic oxidation of m-nitrophenol, Electrochim. Acta 335 (2020), 135649, https://doi.org/10.1016/j.electacta.2020.13564.

[41] Y. Yuan, K. Sheng, S. Zeng, X. Han, L. Sun, I. Loncaric, W. Zhan, D. Sun, Engineering Cu/TiO2@ N-doped C interfaces derived from an atom-precise heterometallic CuII4TiIV5 cluster for efficient photocatalytic hydrogen evolution, Inorg. Chem. 59 (2020) 5456–5462, https://doi.org/10.1021/acs.inorgchem.0c00084.

[42] C. Byrne, L. Moran, D. Hermosilla, N. Merayo, Á. Blanco, S. Rhatigan, S. Hinder, P. Ganguly, M. Nolan, S.C. Pillai, Effect of Cu doping on the anatase-to-rutile phase transition in TiO2 photocatalysts: theory and experiments, Appl. Catal. B Environ. 246 (2019) 266–276, https://doi.org/10.1016/j.apcatb.2019.01.058.

[43] K. Izutsu, Electrochemistry in Nonaqueous Solutions, John Wiley & Sons, 2009.

[44] Q. Dai, Y. Xia, J. Chen, Mechanism of enhanced electrochemical degradation of highly concentrated aspirin wastewater using a rare earth La-Y co-doped PbO2 electrode, Electrochim. Acta 188 (2016) 871–881, https://doi.org/10.1016/j.electacta.2015.10.120.

[45] A. Korent, K.Ž. Soderžnik, S. Šturm, K.Ž. Rožman, A correlative study of polyaniline electropolymerization and its electrochromic behavior, J. Electrochem. Soc. 167 (2020), 106504, https://doi.org/10.1149/1945-7111/ab9929.

[46] M.H. Parvin, M. Pirnia, J. Arjomandi, Electrochemical synthesis, in situ spectroelectrochemistry of conducting indole-titanium dioxide and zinc oxide polymer nanocomposites for rechargeable batteries, Electrochim. Acta 185 (2015) 276–287, https://doi.org/10.1016/j.electacta.2015.10.129.

[47] T. Murugesan, R.R. Kumar, Ak Anbalagan, C.-H. Lee, H.-N. Lin, Interlinked polyaniline/ZnO nanorod composite for selective NO2 gas sensing at room temperature, ACS Appl. Nano Mater. 5 (2022) 4921–4930, https://doi.org/10.1021/acsanm.1c04519.

[48] S. Momeni, D. Nematollahi, New insights into the electrochemical behavior of acid orange 7: convergent paired electrochemical synthesis of new aminonaphthol derivatives, Sci. Rep. 7 (2017) 1–10, https://doi.org/10.1007/s10008-005-0686-2.

[49] A.A. Jbarah, R. Holze, A comparative spectroelectrochemical study of the redox electrochemistry of nitroanilines, J. Solid State Electrochem. 10 (2006) 360–372, https://doi.org/10.1007/s10008-005-0686-2.

[50] F. Cases, F. Huerta, P. Garcés, E. Morallón, J. Vázquez, Voltammetric and in situ FTIRS study of the electrochemical oxidation of aniline from aqueous solutions buffered at pH 5, J. Electroanal. Chem. 501 (2001) 186–192, https://doi.org/10.1016/S0022-0728(00)00526-X.

[51] A. Jannakoudakis, P. Jannakoudakis, N. Pagalos, E. Theodoridou, Electro-oxidation of aniline and electrochemical behaviour of the produced polyaniline film on carbon-fibre electrodes in aqueous methanolic solutions, Electrochim. Acta 38 (1993) 1559–1566, https://doi.org/10.1016/0013-4686(93)80290-G.

[52] A. Sadatnabi, N. Mohamadighader, D. Nematollahi, Convergent paired electrochemical synthesis of azoxy and azo compounds: an insight into the reaction mechanism, Org. Lett. 23 (2021) 6488–6493, https://doi.org/10.1021/acs.orglett.1c02304.

[53] A.J. Bard, L.R. Faulkner, H.S. White, Electrochemical Methods: Fundamentals and Applications, John Wiley & Sons, 2022.